High-speed, low-photodamage nonlinear imaging using passive pulse splitters

Na Ji, Jeffrey C Magee & Eric Betzig

Pulsed lasers are key elements in nonlinear bioimaging techniques such as two-photon fluorescence excitation (TPE) microscopy. Typically, however, only a percent or less of the laser power available can be delivered to the sample before photoinduced damage becomes excessive. Here we describe a passive pulse splitter that converts each laser pulse into a fixed number of sub-pulses of equal energy. We applied the splitter to TPE imaging of fixed mouse brain slices labeled with GFP and show that, in different power regimes, the splitter can be used either to increase the signal rate more than 100-fold or to reduce the rate of photobleaching by over fourfold. In living specimens, the gains were even greater: a ninefold reduction in photobleaching during _in vivo_ imaging of _Caenorhabditis elegans_ larvae, and a six- to 20-fold decrease in the rate of photodamage during calcium imaging of rat hippocampal brain slices.

Ultrafast pulsed lasers have been widely used for nonlinear optical measurements in fields ranging from material characterization to bioimaging. A characteristic common to most such measurements is the small excitation cross-sections involved, resulting in weak signals, long data acquisition times and high requisite pulse intensities. Furthermore, such signals cannot be increased arbitrarily by increasing pulse intensity because in many cases photoinduced damage increases even faster with intensity[1,2]. For example, although most common ultrafast systems (Ti:sapphire) offer time-averaged output powers of several watts, TPE imaging in a biological context[3] is usually limited by photodamage to average powers of <10 mW at the sample[4], often yielding less than one detected photon per pulse[3] and wasting over 99% of the available laser power.

One simple expedient to increase the signal rate and hence the speed of data acquisition N-fold is to accelerate the pulse repetition rate N-fold while maintaining the original pulse intensity. This can yield reduced photodamage compared to the more common approach of increasing the pulse intensity while maintaining the original repetition rate. In another limit, detailed below, the rate of photodamage at constant signal can be decreased by increasing pulse repetition rate, provided that the intensity per pulse is decreased appropriately.

Thus, there is substantial motivation to find a method to increase the repetition rate of pulsed laser sources used in nonlinear optical experiments. Ideally, such a method should be simple, compact and require little or no adjustment. It should introduce minimal dispersion, permit repetition rate gains of at least $100\times$, and be adaptable to the large installed base of preexisting lasers and TPE microscopes. We describe a passive pulse splitter that meets these goals, and present results demonstrating its effectiveness in increasing signal and reducing photobleaching and photodamage in TPE imaging of GFP-labeled fixed cortical brain slices and living _C. elegans_ larvae, as well as in Ca^{2+} imaging of hippocampal slices.

RESULTS
Pulse splitter design
Several methods of passive pulse splitting have been described previously, although none have been demonstrated in the context of nonlinear imaging. In one approach[5], every input pulse injected into a Fabry-Perot etalon consisting of two parallel, partially reflective mirrors is split into an infinite series of output pulses of decreasing intensity. This is not optimal for nonlinear imaging because the most intense sub-pulses in the output train dominate both the signal and the damage. Furthermore, a substantial fraction of the available power is reflected backwards to the source rather than forward to the sample. A related device, termed an optical rattler, uses a parallel stack of etalons of differing reflectivity to equalize the intensity of some of the sub-pulses produced from each input pulse[6,7]. However, other sub-pulses are not equalized, and the task of creating and aligning the multiple surfaces, each with a unique reflectivity, is daunting.

The lessons learned are that, in addition to the attributes listed above, the ideal pulse splitter should create a finite number of equal intensity sub-pulses from each input pulse and do so with minimal power loss so that the full power of the laser can be used to achieve large ($>100\times$) repetition rate gains at sub-pulse intensities comparable to the single pulse intensities currently used.

We designed a splitter that satisfies all of the above requirements (**Fig. 1**). The device consists of two parallel transparent regions of differing thicknesses d_0, d_1 and refractive indices n_0, n_1 sandwiched between two reflecting mirrors, and has a partially reflective coating at the interface between the two regions. In its simplest
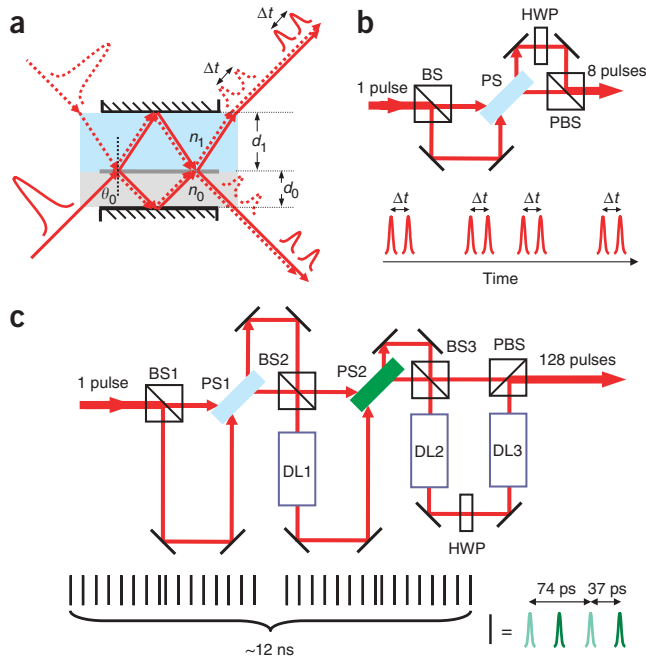
Figure 1 | Construction of pulse splitters. (**a**) A 4× pulse splitter comprising two parallel regions with refractive indices n_0 and n_1, and thicknesses d_0 and d_1. After two pulse splitting events at the partially reflective interface between the two regions, an input pulse incident at angle θ_0 is split into two pairs of pulses with an intra-pair time delay of Δt. Input from both sides of the splitter leads to eight output pulses. (**b**) An 8× pulse splitting configuration with single input/output (top) and the temporal sequence of output pulses (bottom). PS, pulse splitter; BS, beamsplitter; HWP, half-wave plate; PBS, polarizing beamsplitter. (**c**) A 128× pulse splitting configuration comprised of two 4× pulse splitters, PS1 ($\Delta t = 74$ ps) and PS2 ($\Delta t = 37$ ps) (top), and the temporal sequence of output pulses (bottom). Each vertical line represents four pulses having an inter-pulse delay time of 37 ps. DL, delay line.

we chose low dispersion fused silica ($n_1 = 1.453$ at 800 nm) and air ($n_0 = 1$) for the upper and lower regions of the splitters used here. Even so, dispersion sets practical limits on N and Δt: a pulse of 140 fs initial width (typical of Ti:sapphire lasers) traveling through ~50 cm of fused silica (corresponding to $N \cdot \Delta t$ of ~5.1 ns; **Supplementary Methods** online) will face 10^4 fs² of GDD and broaden to ~240 fs. However, as GDD-driven pulse broadening decreases with increasing initial pulse width, splitters can be designed for picosecond or longer pulsed sources with $N \cdot \Delta t$ of ~500 ns or more, although N will also be limited by the tolerances on the parallelism of the surfaces within the splitter ($\leq 50/N$ arcsec) necessary for all sub-pulses to reach the same focal point.

Although a single monolithic pulse splitter with N of ~50 is within the capabilities of modern fabrication methods, we chose a more modular approach (**Fig. 1c**) relying on the serial arrangement of delay lines and splitters of smaller N and differing Δt for this study. By adding or subtracting elements, this approach permitted the relationship between signal and photodamage to be studied as a function of both the pulse repetition rate and the overall splitting ratio.

This system (**Fig. 1c**) consisted of two splitters, of $\Delta t = 74$ ps and $\Delta t = 37$ ps, that produce four sub-pulses for every input pulse. By injecting pulses into both input ports of each splitter, with the second splitter receiving the output of the first, 64 sub-pulses are produced from the original input. A final step of beamsplitting, pulse delay and recombination then leads to 128 pulses arranged in thirty-two groups of four pulses, with an intra-group spacing $\Delta t = 37$ ps, distributed throughout the 12.5 ns interval between laser input pulses (**Fig. 1c**). Removal of various elements leads to five different test configurations (see **Supplementary Figs. 3** and **4** online): $N = 8$, $\Delta t_{\min} = 37$ ps; $N = 8$, $\Delta t_{\min} = 74$ ps; $N = 8$, $\Delta t_{\min} > 1$ ns; $N = 64$, $\Delta t_{\min} = 37$ ps; and $N = 128$, $\Delta t_{\min} = 37$ ps, where $\Delta t_{\min}$ is the minimum time delay between sub-pulses.

Pulse splitting increases TPE imaging speed

To explore the possible benefits of pulse splitting, we used the modular splitter assembly (**Fig. 1**) in conjunction with a TPE microscope to image fixed mouse cortical brain slices expressing cytosolic GFP in a subset of neurons at 910 nm (**Fig. 2**). In the first experiment, we took images with (**Fig. 2a,d**) and without (**Fig. 2b,e**) the splitter in its 64-pulse configuration. Identical energies of ~0.75 pJ/pulse in the two cases were insured by delivering 64× more average power to the sample when we used the splitter.

In the limit where the pulse energy delivered per pixel was sufficiently low and the GFP concentration was sufficiently high
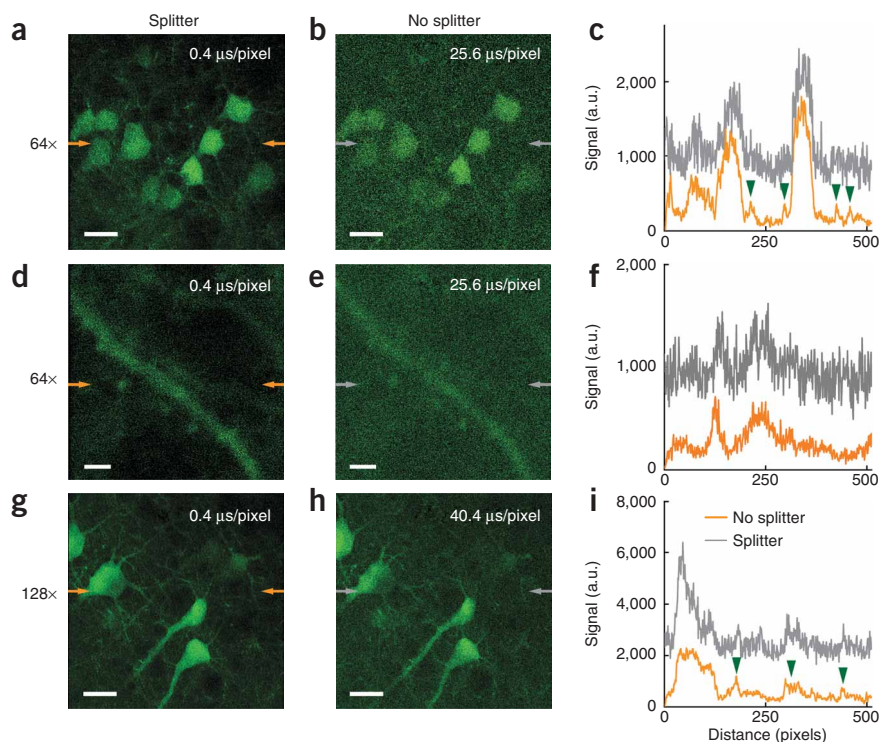
embodiment (**Fig. 1a**), an input pulse injected into the device with an incidence angle θ_0 at the interface is divided by a 50% reflective interfacial coating into two sub-pulses, each of which is divided again after one bounce off of either the top or bottom mirror. The result is four output sub-pulses, one pair emerging from just beyond each of the two mirrors, with an intra-pair pulse spacing time of

$$\Delta t = \frac{2}{c}\sqrt{(n_1^2 - n_0^2)(d_1^2 - d_0^2)},$$

where c is the speed of light. Sub-pulses emerging in the same direction will be spatially overlapped if θ_0 satisfies:

$$\cos\theta_0 = \frac{d_0}{n_0}\sqrt{\frac{n_1^2 - n_0^2}{d_1^2 - d_0^2}},$$

a condition that can be met even with loose tolerances on d_0, d_1 if the splitter is mounted on a rotational stage.

By injecting a second input pulse just before the upper mirror (**Fig. 1a**), four more sub-pulses can be created. A complete eight pulse splitter can then be assembled (**Fig. 1b**) by: (a) dividing a single pulsed input beam with a beamsplitter; (b) guiding each of the resulting beams, with one beam time-delayed with respect to the other, into the two input ports of the splitter; and (c) recombining the two beams emerging from the output ports of the splitter, again with one beam time-delayed with respect to the other, using a half-wave plate and a polarizing beamsplitter. With appropriate delays, none of the eight pulses will overlap in time, yielding a single output beam of 8× higher repetition rate having the pulse characteristics illustrated in **Figure 1b**. This approach can be readily extended to yield N pulses from each output port for a single input, using a splitter having N interfacial bounces (**Supplementary Figs. 1** and **2** online).

Because different frequency components of a laser pulse travel at different velocities in a dispersive material, group-delay dispersion (GDD) leads to pulse-width broadening[8,9]. To minimize such dispersion while maximizing the path length differential (and hence the number of sub-pulses N and/or their separation Δt),

Figure 2 | Pulse splitting increases TPE signal rates. (**a–i**) Comparative two-photon imaging speeds for fixed GFP-labeled brain slices measured with (**a,d,g**) and without (**b,e,h**) pulse splitting, and corresponding comparative line profiles (**c,f,i**) along the arrows shown at left and center (15 pixel averages). Images are not encoded with the same color code (see line profiles). Green arrows in **c** and **i** indicate small neuronal processes that were more readily detected with pulse splitting owing to the presence of background. Measurement conditions (pulse splitting ratio, pixel dwell time, average power at sample): **a,d**, 64×, 0.4 μs, 3.9 mW; **b,e**, none, 25.6 μs, 0.06 mW; **g**, 128×, 0.4 μs, 12.3 mW; and **h**, none, 40.4 μs, 0.11 mW. Scale bars, 20 μm in **a,b,g,h** and 2 μm in **d,e**.

at the same signal rate, an N-pulse splitter requires $N^{1-1/\alpha}$ greater average power but reduces the nonlinear photodamage by $N^{1-\beta/\alpha}$ (see **Supplementary Methods**).

To test this model, we performed TPE line scans with and without the splitter in neighboring regions of the same GFP-labeled soma in a fixed brain slice and recorded the rate of decay of the fluorescence signal. We tested all five splitter configurations illustrated in **Supplementary Fig. 3**, covering splitting ratios of $N = 8$, 64 and 128. The average power P_N required to achieve a constant signal rate scaled as $N^{1/2}$ (**Fig. 3a**), as expected for TPE. This provided further indirect evidence of the uniformity of the pulse intensities provided by the splitter.

for neither saturation to occur nor bleaching to be significant, a 64× increase in signal rate should be observed with the splitter. This was indeed the case: we obtained comparable signals even though the imaging speed of 0.4 μs/pixel with the splitter was 64 times faster than that without the splitter (**Fig. 2**). This also provides indirect confirmation that the splitter produced pulses of approximately equal intensity. Tests with a 128× splitter (**Fig. 1c**) yielded proportionally larger gains (**Fig. 2g,h**). Note the similarity in the resolution with and without the pulse splitter (**Fig. 2d–f**), which indicates that the device was effective in producing spatially overlapped, copropagating sub-pulses.

Pulse splitting reduces photobleaching of fixed GFP

For many optical processes, including TPE fluorescence, photoinduced bleaching and damage increase even more rapidly with increasing excitation intensity I than does the signal generated[1,2,4]. A simple model suggests that in such cases pulse splitting can be used to reduce the rate of photobleaching and photodamage at a given signal level. Consider an optical process of signal $S \propto I^\alpha$ and damage $D \propto I^\beta$, where $\beta > \alpha > 1$. It can be shown that,

Figure 3 | Effect of pulse splitting on photobleaching of fixed GFP-labeled brain slices. (**a**) Ratio of average power required to obtain the same signal rate from GFP-labeled brain sections with and without pulse splitting, for splitting ratios of $N = 8$, 64 and 128. Results conformed to the $N^{1/2}$ dependence expected of two-photon fluorescence. (**b**) Typical data of photobleaching versus time, with and without 128× splitting. Black curves represent double exponential decay fits to the data. With splitting, $T_1 = 45$ s and $T_2 = 109$ s; without splitting, $T_1 = 11$ s and $T_2 = 53$ s. (**c**) Summarized ratios of photobleaching decay times T_1 and T_2 with and without splitting for the five different pulse splitting configurations shown in **Supplementary Figure 3**. Error bars represent s.d. inferred from multiple measurements ($N > 5$). β values derived from these ratios reflect the exponential dependence of the bleaching of fixed GFP on intensity (that is, $D \propto I^\beta$).
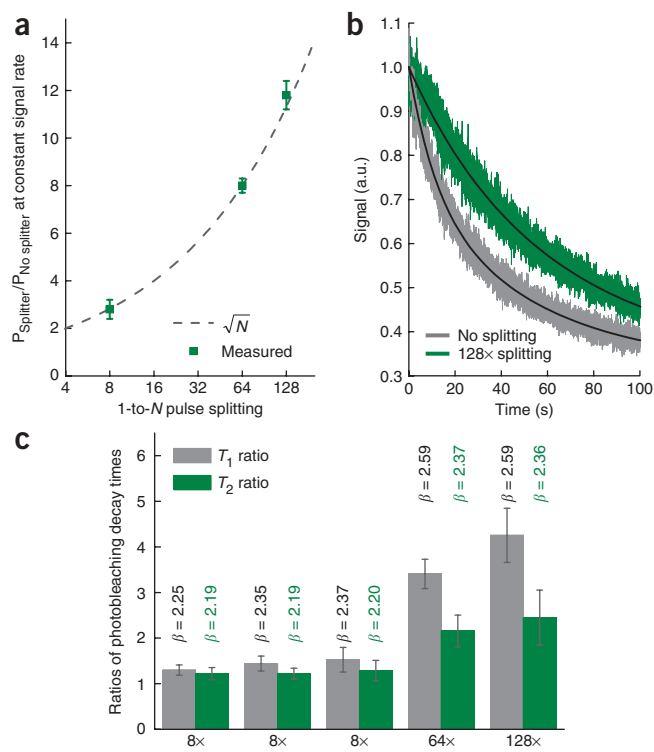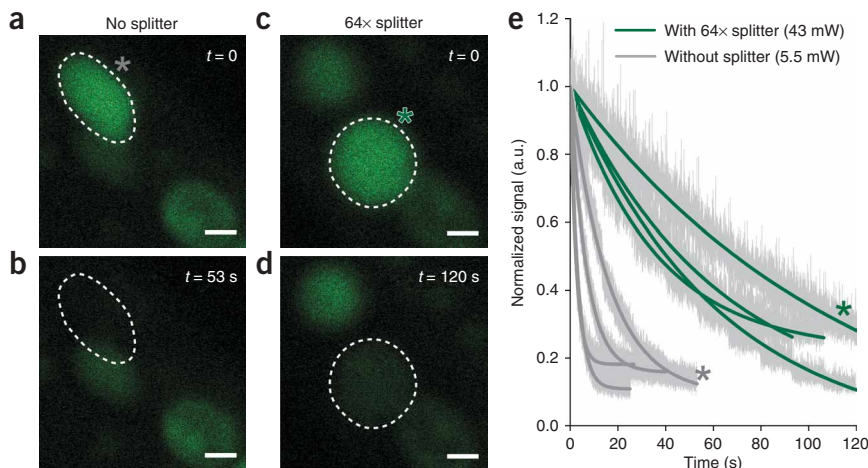
Figure 4 | Effect of $64\times$ pulse splitting on *in vivo* photobleaching in a GFP-labeled *C. elegans* larva. (**a**–**d**) Images of muscle cells before (**a,c**) and after (**b,d**) GFP photobleaching. Cells subjected to bleaching both with (**c,d**) and without (**a,b**) pulse splitting are marked with dashed white curves. (**e**) Normalized photobleaching curves (light gray traces) obtained by repeated line scans over single muscle cells, fit with single exponential decay curves (solid green and dark gray lines). The curves obtained from the cells in **a** and **c** are labeled with gray and green asterisks, respectively. Scale bars, 1 μm.

Typical curves of photobleaching are illustrated in **Figure 3b**. A double-exponential decay formula,

$$S = S_0 + S_1 e^{-t/T_1} + S_2 e^{-t/T_2},$$

was needed to fit the photobleaching data accurately. The shorter decay time T_1 describes the precipitous drop of fluorescence intensity observed at the beginning of the excitation, and T_2 depicts the bleaching on a longer time scale. We measured the ratio of the decay time with the splitter to that without the splitter for both T_1 and T_2 in all five splitter configurations (**Fig. 3c**). Average power was ~ 1 mW at the sample without the splitter and $\sim N^{1/2}$ mW otherwise.

In every configuration and on both time scales, inclusion of the splitter reduced the rate of photobleaching at constant signal. The largest gains occurred for T_1 (for example, $> 4\times$ with the $128\times$ splitter). Furthermore, both T_1 and T_2 continued to improve with increasing N up to the largest value tested ($N = 128$), suggesting that additional gains might be obtained with next-generation splitters of even larger splitting ratios. A damage exponent β between 2.2 and 2.6 can be inferred from these results (**Fig. 3c**).

A major concern during the initial design of the experiment was that splitters with sub-pulse separations Δt considerably shorter than the ~ 3 ns fluorescence lifetime of GFP[10] might actually result in much faster photobleaching owing to the possibility that TPE bleaching is dominated by the absorption of additional photons from molecules already in the excited state. However, the relative independence of the bleaching ratios for both T_1 and T_2 when we used $8\times$ splitters of $\Delta t_{min} = 37$ ps, 74 ps and >1 ns suggests that this concern is not warranted for the power levels and GFP concentration used here. Consequently, it should indeed be feasible to develop splitters with considerably higher splitting ratios because comparatively small (~ 10–50 ps) pulse separations Δt can be used, leading to large values of N before GDD-driven pulse broadening becomes substantial.

Pulse splitting reduces *C. elegans* photobleaching *in vivo*

To assess the effect of pulse splitting in living specimens, we measured GFP photobleaching in muscle cells of *C. elegans* strain PD4251 (ref. 11). We paralyzed *C. elegans* larvae using 50 mM 2,3-butanedione monoxime, held them stationary on 2% agar and performed repeated line scans over individual muscle cells with and without a $64\times$ pulse splitter until the fluorescence signal was largely depleted in each case. We used an average power $8\times$ higher with the splitter to yield similar signal rates in the two cases. We collected images of each muscle cell before and after bleaching (**Fig. 4a–d**), and compared normalized photobleaching curves measured from four cells under each experimental condition (**Fig. 4e**).

Because of the differences in cell size and GFP expression level, both the initial TPE signal and photobleaching dynamics varied from cell to cell. However, the initial TPE signal measured with and without pulse splitting was comparable (**Supplementary Fig. 5** online). The normalized photobleaching curves in **Fig. 4e** clearly demonstrate the benefits of pulse splitting: a GFP-labeled cell was still visible after 120 s with splitting (**Fig. 4c,d**), but another was completely bleached after only 50 s without (**Fig. 4a,b**).

In contrast to the fixed slice measurements, each *in vivo* photobleaching curve could be well-fit assuming a single exponential decay. The average photobleaching rate with 64x pulse splitting decreased ~ 9-fold, from which a bleaching exponent $\beta \sim 3$ can be inferred. Thus, the benefit of pulse splitting is larger than the fixed GFP case in **Fig. 3**, perhaps owing to the higher concentration and mobility of oxygen in living specimens. In addition, the effect of photoinduced heating is minimal[12], since pulse splitting at an average power of 43 mW led to less bleaching than an average power of 5.5 mW without splitting.

Pulse splitting reduces photodamage in Ca²⁺ imaging

A particularly important application of TPE microscopy in neuroscience is imaging of neural activity using Ca^{2+} indicators. In this application, the Ca^{2+} indicator concentration is sufficiently high and its diffusion is sufficiently fast that photodamage affects experiments more than photobleaching. During a typical experiment, the basal fluorescence level F increases with exposure time, and $\Delta F/F$, the relative fluorescence intensity change upon neuronal activity, decreases with time[13]. Prolonged exposure also often leads to severe morphological changes such that the viability of dendrites and spines undergoing measurement ultimately limits the quantity and quality of the collected traces. Here again photodamage is known to have a higher than second-order dependence on excitation intensity[4,13], so pulse splitting should prove beneficial.

To test this, we performed Ca^{2+} imaging experiments on CA1 pyramidal neurons in 400-μm-thick acute rat hippocampal slices at physiological temperature[14]. Using whole-cell patch-clamp pipettes we filled neurons with 200 μM Oregon Green BAPTA-1. We limited all recordings to dendritic regions within 150 μm of the soma and for comparison used separate dendrites within the same focal plane.
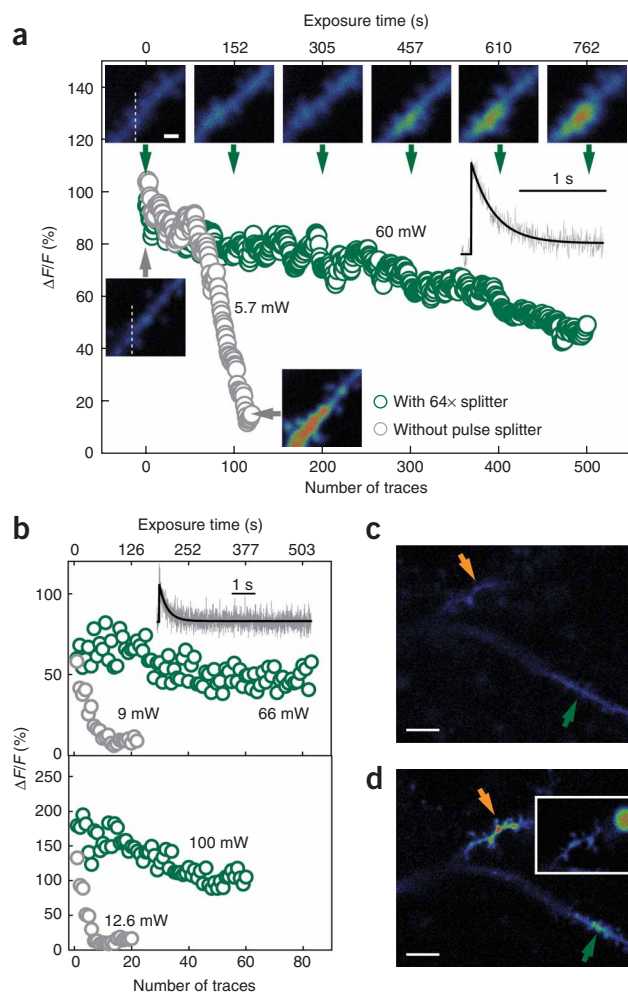
Figure 5 | Effect of 64× pulse splitting on photodamage during Ca²⁺ imaging of CA1 pyramidal neurons injected with Oregon Green BAPTA-1. (**a**) Normalized fluorescence signal change ΔF/F during Ca²⁺ transient traces versus the number of traces and exposure time, as measured from two dendritic branches of a single neuron, one with 64× pulse splitting and one without, at two average powers as shown. Inset curve, a typical 1.57s Ca²⁺ transient trace. Inset images are basal fluorescence images of the dendrites taken during the measurements, with arrows indicating the time points at which they were taken and dashed lines indicating the locations of line scans. (**b**) ΔF/F measured for longer Ca²⁺ transient traces (inset curve) and at higher average powers. (**c**) Basal fluorescence image before Ca²⁺ imaging of the dendritic branches from which the data in the upper panel of **b** were obtained. (**d**) The same area as in **c** after Ca²⁺ imaging. The upper branch (orange arrows) was traced 10 times without pulse splitting and the lower branch (green arrows) was traced 80 times with 64× splitting. Inset, upper branch after 12 traces without pulse splitting. Scale bars, 1 μm in **a**, 5 μm in **c** and **d**.

We induced two back-propagating action potentials by somatic current injection, and detected the Ca²⁺ transient in dendrites and spines by rapid line scans using 830-nm excitation (see **Supplementary Methods** for details). We chose ΔF/F as the metric of photodamage, and measured the dependence of ΔF/F on accumulated exposure time with and without a 64× pulse splitter.

We measured the temporal evolution of ΔF/F from two dendritic branches of a single neuron in response to repeated action potential initiation, with a 64× splitter and without (**Fig. 5a**). We used average powers of 60 mW and 5.7 mW post objective with and without the 64× splitter, respectively. The former power was chosen intentionally high and yielded a higher basal fluorescence signal (**Supplementary Fig. 6** online). Although this skews the photodamage comparison in favor of the no-splitter scenario, the pulse splitter still drastically reduced photodamage. Without pulse splitting, ΔF/F decreased rapidly after ∼75-s exposure (50 traces), and after 120 traces, the basal fluorescence increased ∼7×, whereas ΔF/F dropped to 10% of its original value. At this point, the experiment had to be terminated to prevent destroying the dendrite. In comparison, with the 64× pulse splitter, the basal fluorescence increased much more slowly: after >700s exposure (500 traces), ΔF/F only dropped to half its original value. Defining the Ca²⁺ imaging 'lifetime' as the number of traces required for ΔF/F to decrease by one-half, we found that a 6× gain in lifetime was afforded by the use of a 64× splitter, despite the higher initial basal signal.

We also explored other experimental parameters by collecting longer traces (6.28-s traces every 17 s) and using higher average powers (**Fig. 5b–d**). Both with and without pulse splitting, higher average power led to faster photodamage, as expected. However, given similar basal fluorescence (**Supplementary Fig. 6**), pulse splitting always improved the Ca²⁺ imaging lifetime, with more dramatic gains occurring at increasingly high power (>10× at 66 mW and >20× at 100 mW; **Fig. 5b**).

We collected basal fluorescence images before and after Ca²⁺ imaging of the two sister branches used to obtain the data in the upper panel of **Figure 5b** (**Fig. 5c,d**). After 10 traces without pulse splitting, the upper branch showed substantial damage, as indicated by its much elevated basal fluorescence. After two more traces, a brightly fluorescent vesicular structure appeared along the branch. In contrast, with pulse splitting, the elevation of basal fluorescence in the lower branch was only moderately higher even after 80 traces, and ΔF/F was still above half maximum. Similar to the *C. elegans* measurements, damage owing to heating by one-photon absorption was not noticeable up to 100 mW when we used the 64× pulse splitter, although such heating effects may prove deleterious for other samples or other imaging conditions.

DISCUSSION

We demonstrated the efficacy of pulse splitting for enhancing signal and reducing photobleaching and photodamage in TPE microscopy. The same principle can be applied to other multiphoton imaging methods, including those based on second harmonic generation[15], sum frequency generation[16,17] and coherent anti-Stokes Raman scattering[18]. These benefits may also hold for single-molecule TPE microscopy[19].

Other means to similar ends have also been reported. For example, a femtosecond laser with a 2 GHz repetition rate has been used to improve imaging speed and minimize photodamage in second harmonic generation microscopy[20]. Unfortunately, these systems generally have limited power (∼500 mW) and tunability (±10 nm). Fast TPE imaging has also been demonstrated with multifocal multiphoton microscopy, where microlens arrays[21,22], etalons[23], beamsplitters[24] or diffractive optical elements[25] are used to partition a considerable fraction of the total available laser energy in an array of foci within the sample and multi-element detectors[26] are used to detect the fluorescence produced. However, in strongly scattering tissues where TPE is often advantageously applied, multifocal multiphoton microscopy image quality deteriorates

rapidly with depth owing to detection channel cross-talk caused by the intense scattering of the fluorescence emission[26].

Viewed in this context, the pulse splitter approach demonstrated here offers several substantial advantages. It is compact, requires few adjustments and can be added to any existing pulsed laser or TPE microscope. It can be flexibly reconfigured to optimize the repetition rate, pulse spacing and pulse intensity based on the photophysics of the system under investigation. By coaxing higher signal rates from a single focus, it is well suited to increase data acquisition rates for many nonlinear optical applications. When reduced photoinduced bleaching and damage are paramount, pulse splitting can greatly increase the total integrated signal obtainable from various sample preparations, ranging from GFP in fixed tissues and living *C. elegans* larvae, to Ca^{2+} indicators in acute brain slices.

METHODS

Imaging experiments. For all experiments we used a commercial TPE microscope (Ultima; Prairie Technologies) equipped with a 60×, 0.9 numerical aperture (NA) water immersion objective (LUMPlanFI/IR; Olympus) and an 80 MHz Ti:sapphire laser (Cameleon; Coherent Inc.). Laser power was measured after the objective and controlled by a Pockels cell (model 302; Conoptics). We carried out line scan measurements at 2 ms per 1.6 µm line. We performed all GFP imaging and bleaching measurements at 910 nm and all calcium imaging experiments at 830 nm.

Additional methods. Sample preparation (fixed mouse brain slices, rat hippocampal brain slices and GFP-expressing *C. elegans* larvae), pulse splitter design parameters, various pulse splitting configurations, and additional data on the *C. elegans* and Ca^{2+} imaging experiments are available in **Supplementary Methods**. All experiments were performed according to methods approved by the Janelia Farm Institutional Animal Care and Use Committee.

Note: Supplementary information is available on the Nature Methods website.

**Published online at http://www.nature.com/naturemethods/
Reprints and permissions information is available online at
http://npg.nature.com/reprintsandpermissions**

1. Chen, T.S. *et al.* High-order photobleaching of green fluorescent protein inside live cells in two-photon excitation microscopy. *Biochem. Biophys. Res. Commun.* **291**, 1272–1275 (2002).

2. Patterson, G.H. & Piston, D.W. Photobleaching in two-photon excitation microscopy. *Biophys. J.* **78**, 2159–2162 (2000).

3. Denk, W., Strickler, J.H. & Webb, W.W. Two-photon laser scanning fluorescence microscopy. *Science* **248**, 73–76 (1990).

4. Hopt, A. & Neher, E. Highly nonlinear photodamage in two-photon fluorescence microscopy. *Biophys. J.* **80**, 2029–2036 (2001).

5. Sizer, T., II Increase in laser repetition rate by spectral selection. *IEEE J. Quantum Electron.* **25**, 97–103 (1989).

6. MacFarlane, D.L., Strozewski, K.J. & Tatum, J.A. Mode-locked laser pulse train repetition frequency multiplication: the optical rattler. *Appl. Opt.* **30**, 1042–1047 (1991).

7. Narayan, V., Dowling, E.M. & MacFarlane, D.L. Design of multimirror structures for high-frequency bursts and codes of ultrashort pulses. *IEEE J. Quantum Electron.* **30**, 1671–1679 (1994).

8. Guild, J.B., Xu, C. & Webb, W.W. Measurement of group delay dispersion of high numerical aperture objective lenses using two-photon excited fluorescence. *Appl. Opt.* **36**, 397–401 (1997).

9. Squier, J. & Muller, M. High resolution nonlinear microscopy: A review of sources and methods for achieving optimal imaging. *Rev. Sci. Instrum.* **72**, 2855–2867 (2001).

10. Volkmer, A. *et al.* One- and two-photon excited fluorescence lifetimes and anisotropy decays of green fluorescent proteins. *Biophys. J.* **78**, 1589–1598 (2000).

11. Fire, A. *et al.* Potent and specific genetic interference by double-stranded RNA in *Caenorhabditis elegans*. *Nature* **391**, 806–811 (1998).

12. Schonle, A. & Hell, S.W. Heating by absorption in the focus of an objective lens. *Opt. Lett.* **23**, 325–327 (1998).

13. Koester, H.J. *et al.* Ca^{2+} fluorescence imaging with pico- and femtosecond two-photon excitation: signal and photodamage. *Biophys. J.* **77**, 2226–2236 (1999).

14. Magee, J.C. Dendritic Ih normalizes temporal summation in hippocampal CA1 neurons. *Nat. Neurosci.* **2**, 508–514 (1999).

15. Campagnola, P.J. *et al.* High-resolution nonlinear optical imaging of live cells by second harmonic generation. *Biophys. J.* **77**, 3341–3349 (1999).

16. Florsheimer, M., Brillert, C. & Fuchs, H. Chemical imaging of interfaces by sum frequency microscopy. *Langmuir* **15**, 5437–5439 (1999).

17. Ji, N. *et al.* Three-dimensional chiral imaging by sum-frequency generation. *J. Am. Chem. Soc.* **128**, 3482–3483 (2006).

18. Zumbusch, A., Holtom, G.R. & Xie, X.S. Three-dimensional vibrational imaging by coherent anti-stokes raman scattering. *Phys. Rev. Lett.* **82**, 4142 (1999).

19. Mertz, J., Xu, C. & Webb, W.W. Single-molecule detection by two-photon-excited fluorescence. *Opt. Lett.* **20**, 2532–2534 (1995).

20. Chu, S.W., Liu, T.M. & Sun, C.K. Real-time second-harmonic-generation microscopy based on a 2-GHz repetition rate Ti:sapphire laser. *Opt. Exp.* **11**, 933–938 (2003).

21. Bewersdorf, J., Pick, R. & Hell, S.W. Multifocal multiphoton microscopy. *Opt. Lett.* **23**, 655–657 (1998).

22. Buist, A.H. *et al.* Real time two-photon absorption microscopy using multi point excitation. *J. Microsc. (Oxf.)* **192**, 217–226 (1998).

23. Fittinghoff, D.N. & Squier, J.A. Time-decorrelated multifocal array for multiphoton microscopy and micromachining. *Opt. Lett.* **25**, 1213–1215 (2000).

24. Fricke, M. & Nielsen, T. Two-dimensional imaging without scanning by multifocal multiphoton microscopy. *Appl. Opt.* **44**, 2984–2988 (2005).

25. Sacconi, L. *et al.* Multiphoton multifocal microscopy exploiting a diffractive optical element. *Opt. Lett.* **28**, 1918–1920 (2003).

26. Kim, K.H. *et al.* Multifocal multiphoton microscopy based on multianode photomultiplier tubes. *Opt. Exp.* **15**, 11658–11678 (2007).